



HAL
open science

Embedded Ni nanoparticles in CeZrO₂ as stable catalyst for dry reforming of methane

André L.A. Marinho, Raimundo C. Rabelo-Neto, Florence Epron, Nicolas Bion, Fabio S. Toniolo, Fabio Bellot Noronha

► To cite this version:

André L.A. Marinho, Raimundo C. Rabelo-Neto, Florence Epron, Nicolas Bion, Fabio S. Toniolo, et al.. Embedded Ni nanoparticles in CeZrO₂ as stable catalyst for dry reforming of methane. Applied Catalysis B: Environmental, 2020, 268, pp.118387. 10.1016/j.apcatb.2019.118387. hal-02903461

HAL Id: hal-02903461

<https://hal.science/hal-02903461>

Submitted on 27 Nov 2020

HAL is a multi-disciplinary open access archive for the deposit and dissemination of scientific research documents, whether they are published or not. The documents may come from teaching and research institutions in France or abroad, or from public or private research centers.

L'archive ouverte pluridisciplinaire **HAL**, est destinée au dépôt et à la diffusion de documents scientifiques de niveau recherche, publiés ou non, émanant des établissements d'enseignement et de recherche français ou étrangers, des laboratoires publics ou privés.

Embedded Ni nanoparticles in CeZrO₂ as stable catalyst for dry reforming of methane

André L. A. Marinho^{1,2,3}, Raimundo C. Rabelo-Neto², Florence Epron³, Nicolas Bion³, Fabio
S. Toniolo¹, Fabio B. Noronha^{2,*}

¹ Federal University of Rio de Janeiro, Chemical Engineering Program of COPPE/UFRJ, P.O.
Box 68502, CEP 21941-972, Rio de Janeiro, RJ, Brazil.

² National Institute of Technology, Catalysis Division, Rio de Janeiro, RJ 20081-312, Brazil.

³ University of Poitiers, Institut de Chimie des Milieux et Matériaux de Poitiers (IC2MP),
TSA51106 – F86073 Poitiers Cedex 9, France

* Corresponding author: fabio.bellot@int.gov.br

Submitted to Applied Catalysis B: Environmental

Revised November 2019

Abstract

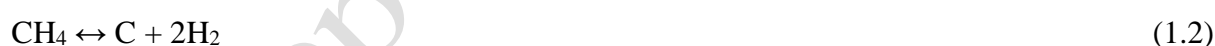
Ni nanoparticles embedded in CeO₂ (Ni@CeO₂) and CeZrO₂ (Ni@CeZrO₂) were synthesized by sol-gel method and compared with a Ni/CeO₂ prepared by support impregnation. The performance of the catalysts was investigated for dry reforming of methane reaction. In situ XRD, XANES and TEM showed that Ni embedded in CeO₂ improved the resistance to sintering along the reduction at 800°C. Doping ceria with zirconia inhibited the growth of Ni particles and increased the oxygen mobility. SEM, TEM, Raman spectroscopy and TGA of the used catalysts after dry reforming of methane showed that carbon formation rate was significantly reduced for the catalysts containing Ni nanoparticles embedded in ceria structure. Carbon deposits were not detected over Ni@CeZrO₂ after 24 h of reaction. Therefore, the control of Ni particle size and the high oxygen mobility of Ni@CeZrO₂ catalyst inhibited carbon deposition and favored the mechanism of carbon removal, promoting catalyst stability.

Key words: Ni-embedded; Ceria; Ceria-Zirconia; Oxygen Isotopic Exchange; Methane Dry Reforming; Biogas.

1- Introduction

Biogas obtained by anaerobic digestion of biomass is a source of CH₄ and CO₂ and it can be regarded as an alternative renewable source of methane. Nowadays, the biogas produced from biomass waste in the farms is mostly used to produce thermal or electrical energy. However, biogas can be used for the production of renewable energy and added-value chemicals [1]. Hydrogen produced via biogas reforming might be used for energy generation on low-temperature fuel cells or it can be directly fed to high-temperature fuel cells [2-5].

Steam reforming of methane is the main industrial process to produce H₂. However, the dry reforming of methane (DRM) (Eq. 1.1), using directly the biogas as feedstock, could be an alternative for obtaining hydrogen [6]. The main limitation of DRM technology is catalyst deactivation due to carbon deposition, which occurs under reaction conditions. DRM is an endothermic reaction ($\Delta H^\circ = 247$ kJ/mol) and requires high reaction temperature, which favors several side reactions, especially CH₄ decomposition (Eq. 1.2), Boudouard reaction (Eq. 1.3) and reverse water-gas shift (RWGS) (Eq. 1.4) [7].



The development of catalysts resistant to deactivation by carbon deposition has been the focus of several studies. Supported metal catalysts have been extensively investigated for the DRM [8,9]. Ni-based catalysts have high activity and low cost, but metal sintering may occur during the DRM and thus favor the production of coke on its surface, leading to catalyst deactivation [10].

The high temperature required to perform the DRM favors the metal sintering process, which motivates the development of novel catalysts able to resist to deactivation. Recently, the literature reported a series of catalysts in which the metal phase is embedded into an oxide, improving the catalyst stability by avoiding the metal sintering [11–14]. Ni@SiO₂ [15] and Ni@Al₂O₃ [16] catalysts exhibited high resistance to metal sintering during the DRM but carbon formation was not totally inhibited. The development of metallic Ni particles embedded into oxides with high OSC could combine two advantages: to limit the metal sintering and prevent or remove carbon deposition.

The use of supports with redox properties is reported to improve catalyst stability for the DRM, due to the enhancement of the rate of carbon gasification on the catalyst surface. The use of CeO₂ has been investigated as a support in many reactions, which required high oxygen storage capacity (OSC) [17,18]. As a support for the DRM, ceria participates in the dissociative adsorption of CO₂ and donates an oxygen atom to the metallic particle containing carbon deposits, promoting the carbon removal mechanism [18]. Furthermore, doping ceria structure with appropriate cations can modify the lattice parameters, increasing the amount of oxygen exchangeable species. The literature reports ZrO₂ as an excellent dopant to increase the redox properties of ceria [19–22].

The use of ceria to confine metals has been also investigated [11,23], but the synthesis procedures are quite complex and hardly reproducible with high cost. Recently, Wang et al.[24] synthesized Cu nanoparticles embedded in CeO₂ by a simple sol-gel method. The catalysts were tested for hydrogenation of methyl acetate reaction at 400 °C and no sintering was observed. However, to the best of our knowledge, there is still no report in the literature about this sol-gel method for the synthesis of Ni@CeO₂ catalyst and its application for the DRM.

In this work, we aim to prepare Ni-embedded CeO₂ catalysts using a one-step synthesis method and test them for the DRM. The use of ZrO₂ as dopant was also evaluated. A Ni/CeO₂

catalyst prepared by traditional impregnation method was also tested for comparison. Important structure properties were investigated by Transmission Electron Microscopy, Raman Spectroscopy, in-situ X-ray Diffraction and in-situ X-ray Absorption. The mobility of oxygen in the material was characterized by Oxygen Isotopic Exchange. The carbon formation was analyzed by Thermogravimetric analysis, Raman Spectroscopy, Scanning and Transmission Electron Microscopy.

Accepted manuscript

2. Experimental

2.1. Catalysts preparation

Catalysts were prepared following an adapted method previously described in the literature [24]. A solution of cerium nitrate (1.7 mol.L^{-1} , 25 mL) was prepared, followed by the addition of an appropriate amount of nickel nitrate to obtain 10 wt% Ni in the catalyst. In another beaker, a solution of citric acid (6.7 mol.L^{-1} , 25 mL) was prepared, using a citric acid/metals molar ratio equal to 1.0. Both solutions were mixed and stirred for 2 h at room temperature. Then, the solution was heated at $70 \text{ }^\circ\text{C}$ under vacuum to remove water. The remaining material was dried at $100 \text{ }^\circ\text{C}$ overnight. The calcination occurred in 2 steps: 2 h at $300 \text{ }^\circ\text{C}$ and 4 h at $400 \text{ }^\circ\text{C}$, using a heating rate of $1 \text{ }^\circ\text{C}/\text{min}$. This catalyst was denominated Ni@CeO₂. The zirconia-doped ceria catalyst (Ni@CeZrO₂) was prepared using the same method with the addition of zirconyl nitrate at the metal solution. The Ce/Zr molar ratio was 4.0.

For comparison, a Ni/CeO₂ catalyst was prepared by incipient wetness impregnation of CeO₂ support with an aqueous solution of nickel nitrate. In this case, CeO₂ was synthesized by the method previously described but without the addition of nickel.

2.2. X-ray fluorescence (XRF)

The chemical composition of the catalysts was determined by an X-ray fluorescence spectrometer RIGAKU RIX-3100 using samples as pellet.

2.3. N₂ physisorption

The BET surface area of the samples was measured by N₂ adsorption using a Micromeritics Tristar 3000 apparatus at $-196 \text{ }^\circ\text{C}$. The samples were degassed at $300 \text{ }^\circ\text{C}$ under vacuum before the analysis.

2.4. *Transmission electron microscopy (TEM)*

TEM analyses of reduced and used catalysts were made in a JEOL 2100 UHR apparatus, with 0.19 and 0.14 nm punctual and linear resolution, respectively, equipped with a LaB₆ filament. Energy dispersive X-ray (EDX) analysis was also performed to determine the local chemical composition. The range used to collect the X-rays emitted from the sample upon electron impact was 0 – 20 keV. Before the analysis, the samples were reduced at 800 °C for 1h, the same temperature used for the reaction.

2.5. *In-situ X-ray diffraction (XRD)*

In-situ X-ray diffraction was performed at the XPD-10 B beamline at the Brazilian Synchrotron Light Laboratory (LNLS). The samples were reduced under a 5 % H₂/He mixture at a heating rate of 10 °C/min, from 25 to 800 °C, remaining at the final reduction temperature for 1 h. The XRD patterns were obtained at 2 θ range from 23° to 56° and the wavelength used was 1.55002 Å. The average crystallite size of NiO, metallic Ni and CeO₂ was calculated using the Scherrer equation. The CeO₂ lattice parameter was calculated using the Bragg's Law, assuming an orthorhombic structure and the (111) CeO₂ plane.

2.6. *In-situ X-ray absorption near edge structure (XANES)*

XANES analysis was performed at the DXAS beamline at LNLS to obtain information about the reduction degree of Ni during the reduction procedure. The samples were diluted with boron nitride, used as inert, and pressed to obtain a pellet. The pellet was placed in a tubular reactor and reduced under a 5 % H₂/He mixture up to 750 °C, keeping this temperature for 30 min. The treatment of XANES data was carried out using PrestoPronto software [25]. The

fraction of metallic Ni phase was calculated as a function of reduction temperature by linear combination using NiO and Ni⁰ foil XANES spectra as references.

2.7. ¹⁸O₂/¹⁶O₂ isotopic exchange

The experiments were carried out in a closed recycling system connected to a Pfeiffer Vacuum quadrupole mass spectrometer and a vacuum pump. Firstly, the sample (c.a. 20 mg) was pre-treated under ¹⁶O₂ flow (50 mL/min, 500 °C, 1 h) and evacuated for 1 h. After the pre-treatment, the sample was cooled down to reaction temperature.

For the Isothermal Oxygen Isotopic Exchange (IOIE), the reactions occurred at 350 °C, 400 °C and 450 °C. It was inserted in the reactor 55 mbar of pure ¹⁸O₂ (≥ 99 at.%, ISOTECH) and each isotopomer concentration was analyzed by monitoring the following m/z signals: 32 (¹⁶O₂), 34 (¹⁸O¹⁶O), 36 (¹⁸O₂).

The behavior of the oxygen exchange was studied as a function of the temperature (Temperature-Programmed Oxygen Isotopic Exchange – TPOIE). For this experiment, pure ¹⁸O₂ (55 mbar) was injected in the reactor at 200 °C and the sample was heated up to 500 °C (2 °C/min).

The following equations were used to calculate the rate of exchange (R_E), the number of oxygen exchanged (N_E), where N_g is the total number of oxygen atoms in the gas phase, w is the weight of catalyst, α_g^t is the atomic fraction of ¹⁸O₂ in the gas phase at the time t, α_g⁰ is the initial atomic fraction of ¹⁸O₂ in the gas phase.

$$\alpha_g^t = \frac{1/2 P_{34}^t + P_{36}^t}{P_{36}^t + P_{34}^t + P_{32}^t} \quad R_E = -N_g \frac{d \alpha_g^t}{dt} \times \frac{1}{w}$$

$$N_E = (\alpha_g^0 - \alpha_g^t) \times N_g \times \frac{1}{w}$$

2.8. Raman spectroscopy

The calcined samples were analyzed in a Raman Horiba Jobin Yvon spectrometer using a He:Ne laser (632 nm). The post-reaction samples were analyzed in a Raman Witec – Alpha 300 spectrometer. The 532 nm wavelength was used to observe the carbon structure on the samples.

2.9. Thermogravimetric analysis (TG)

In order to quantify the amount of coke formed on the catalyst, thermogravimetric analyses of the post-reaction samples were carried out in a TA Instruments equipment (SDT Q600). Approximately 10 mg of the spent catalyst was heated under synthetic air flow (100 mL/min) from room temperature to 1000 °C at a heating rate of 20 °C/min and the weight change was measured.

2.10. Scanning electron microscopy (SEM)

SEM analyses of the spent catalysts were carried out using a field emission scanning electron microscope (FE-SEM) Quanta FEG 450 FEI operating with an accelerating voltage of 20 kV.

2.11. Catalytic evaluation

Dry reforming of methane was performed in a fixed-bed reactor at atmospheric pressure. Before the reaction, the catalysts were reduced under pure H₂ (30 mL/min) at 800 °C for 1 h and purged under N₂ at the same temperature for 30 min. A reactant mixture with CH₄:CO₂ molar ratio equal to 1.0 under flow rate of 100 mL/min was used for the DRM at 800 °C.

The samples (20 mg) were diluted with SiC (SiC mass/catalyst mass ratio = 1.5) to avoid hot spot or temperature gradients. The reaction products were analyzed by gas chromatography

(Agilent 6890) equipped with a thermal conductivity detector and Carboxen 1010 column (Supelco). The CH₄ and CO₂ conversion was determined as follow:

$$X_{\text{CH}_4} = \frac{(n_{\text{CH}_4})_{\text{feed}} - (n_{\text{CH}_4})_{\text{exit}}}{(n_{\text{CH}_4})_{\text{feed}}} \times 100$$

$$X_{\text{CO}_2} = \frac{(n_{\text{CO}_2})_{\text{feed}} - (n_{\text{CO}_2})_{\text{exit}}}{(n_{\text{CO}_2})_{\text{feed}}} \times 100$$

Accepted manuscript

3. Results and discussion

3.1. Catalyst characterization

Table 1 shows the Ni content, Ce/Zr molar ratio and the textural properties of the catalysts. The Ni loading is close to the nominal value (10 wt%) for all samples, as well as the Ce/Zr molar ratio of the Ni@CeZrO₂ catalyst (i.e., Ce/Zr = 4). The surface area and pore volume for Ni/CeO₂ and Ni@CeO₂ catalysts were similar but decreased when zirconia was added to ceria. After the reduction process at 800 °C under H₂, the BET surface area dropped to less than 10 m²/g to Ni/CeO₂ and Ni@CeO₂ catalysts. This reduction in the BET surface area can be correlated to sintering of CeO₂ at high temperature [26,27]. The decrease in BET surface area of Ni@CeZrO₂ sample was lower than that for the other samples. According to the literature [28], the addition of Zr into the ceria structure with the formation of a solid solution improves the thermal stability of the ceria support, inhibiting or minimizing sintering and surface area lost at high temperatures.

The TEM images of the reduced Ni/CeO₂, Ni@CeO₂ and Ni@CeZrO₂ catalysts are shown in Fig. 1. The image of Ni/CeO₂ catalyst shows large Ni particle segregated on the surface of the sample, with average particle size around 30 nm. The local chemical analysis showed only the presence of Ni due the large size and CeO₂ could not be detected in the area of analysis (white circle). For Ni@CeO₂ and Ni@CeZrO₂ catalysts, the TEM images reveals the presence of small Ni nanoparticles embedded in the ceria matrix formed during reduction. Segregated Ni particles could not be observed on the TEM images of Ni@CeO₂ and Ni@CeZrO₂ catalysts. Ni-embedded catalysts presented smaller metal particle size than Ni/CeO₂. For Ni@CeO₂ and Ni@CeZrO₂, the Ni particles sizes were around 13 and 6 nm, respectively. It was possible to detect the CeO₂ signal by EDX in the selected area (white circle) due the small Ni particle size and it seems that the nanoparticles embedded in the ceria matrix are protected.

The Raman spectra of the calcined samples are shown in Fig. 2. The spectrum of CeO₂ support is also presented for comparison. The support exhibits only one intense band at 462 cm⁻¹ assigned to the symmetrical stretching mode between the eight oxygen atoms bound to the cerium atom in the triple degenerate F_{2g} mode. The impregnation of ceria with Ni does not affect the spectrum of Ni/CeO₂, but Ni@CeO₂ and Ni@CeZrO₂ samples show a ceria structure completely different from the impregnated one. Besides the intense band around 462 cm⁻¹, the spectra display bands at 224, 544 and 632 cm⁻¹, corresponding to second-order transverse acoustic mode (2TA) and defect-induced mode. These samples exhibited two different defects in the structure, which were reported in the literature as defect space including O²⁻ vacancy (544 cm⁻¹) and defect space without O²⁻ vacancy (632 cm⁻¹) [29,30]. The NiO also presents bands in the region of 570 cm⁻¹ corresponding to TO and LO vibration modes [31]. However, this band is not detected or it has a very weak intensity in the spectrum of Ni/CeO₂ sample. Therefore, the bands observed at 544 cm⁻¹ and 632 cm⁻¹ in the spectra of Ni@CeO₂ and Ni@CeZrO₂ samples might be attributed to oxygen vacancies. Therefore, the one-step synthesis of the catalyst with Ni embedded in the ceria structure can promote the formation of defect in the ceria, creating oxygen vacancies in its structure.

The Raman spectra did not detect the formation of a Ni-CeO₂ solid solution, as described by Barrio et al [32]. The formation of Ni-CeO₂ solid solution significantly shifted the frequency for the first-order F_{2g} peak to lower values, around 445 cm⁻¹. Then, the absence of the shift of this band for the Ni@CeO₂ catalyst shows that the Ni is embedded in CeO₂ structure instead of in a solid solution.

XANES experiments at the Ni K-edge were performed to study the reduction of nickel oxide for all samples (Figs. 3, 4 and 5). The XANES spectrum of the calcined Ni/CeO₂ sample shows the white line at 8352 eV characteristic of NiO. Increasing the reduction temperature under 5 % H₂/He mixture led to a continuous decrease in the intensity of this peak. At 450 °C,

the spectrum is characteristic of metallic Ni, indicating that nickel oxide was completely reduced to Ni⁰. The same trend was observed for Ni@CeO₂ and Ni@CeZrO₂ catalysts as shown in Figs. 4 and 5.

However, the temperature range for the reduction of Ni oxide was different for the catalysts prepared by impregnation and sol-gel methods. Fig. 6 shows the evolution of the metallic Ni species during reduction calculated by the linear combination of Ni K-edge XANES spectra of references. The reduction of Ni/CeO₂ and Ni@CeO₂ samples starts at 290 and 277 °C, respectively, but at 190 °C for Ni@CeZrO₂ catalyst. The total reduction of nickel oxide on Ni/CeO₂ sample is achieved at 450 °C, while the complete reduction of the Ni@CeO₂ and Ni@CeZrO₂ samples occurs at higher temperatures (700 and 530 °C, respectively). The shift of reduction temperature to higher values is likely due to a higher metal-support interaction [32]. Therefore, these results suggest that nickel oxide particles embedded in the CeO₂ or CeZrO₂ matrix have stronger interaction with the support than nickel oxide particles impregnated on CeO₂. Stronger interaction demands higher temperature of reduction to remove oxygen from the oxide structure.

Fig. 7 shows the diffractograms of the calcined samples. Ni/CeO₂ and Ni@CeO₂ samples exhibit the characteristic lines of CeO₂ with fluorite structure (PDF 34-0394) at $2\theta = 28.7^\circ$, 33.2° and 47.7° . The typical lines of NiO phase (PDF 47-1049) ($2\theta = 37.3^\circ$ and 43.3°) are only detected for Ni/CeO₂ sample. The absence of diffraction lines ascribed to NiO phase in the diffractogram of Ni@CeO₂ sample can be attributed to the presence of very small NiO crystallites in this catalyst, indicating that sintering did not occur during the calcination. For Ni@CeZrO₂ sample, the lines characteristic of NiO phase are not detected either whereas the lines corresponding to CeO₂ are shifted to higher 2θ positions. The partial substitution of Ce⁴⁺ by Zr⁴⁺ ions in the ceria structure shifted the CeO₂ lines to higher Bragg angles that corresponds to a decrease in the lattice parameter (Table 2) due to the difference between the

ionic radii of the cations Ce^{4+} (0.97 Å) and Zr^{4+} (0.84 Å) [33]. According to the literature, this shift indicates the formation of a $\text{CeO}_2\text{-ZrO}_2$ solid solution for the Ni@CeZrO_2 catalyst [18,34]. Ni/CeO_2 catalyst exhibited a ceria lattice parameter higher than that one reported in the literature (5.4112 Å), while it further decreased for Ni@CeO_2 with Ni embedded in CeO_2 . The CeO_2 crystallite size of the Ni/CeO_2 sample is 13.4 nm, while a significant decrease is observed for Ni@CeO_2 and Ni@CeZrO_2 catalysts (4.4 and 4.1 nm, respectively) (Table 2). Wang et al. [24] synthesized a Cu@CeO_2 catalyst using the same method and they observed the same effect on ceria crystallite size during calcination.

X-ray diffraction patterns obtained during reduction under 5 % H_2/He mixture from room temperature to 800 °C for Ni/CeO_2 , Ni@CeO_2 and Ni@CeZrO_2 samples are shown in Figs. 8A, 9A and 10A. The evolution of the mean crystallite size of NiO , Ni^0 and CeO_2 during reduction procedure is presented in Figs. 8b, 9b and 10b.

For Ni/CeO_2 catalyst (Fig. 8A), the diffractograms show the decrease in the intensities of the lines corresponding to NiO at $2\theta = 37.3^\circ$ and 43.3° during reduction. Above 300 °C, the typical lines of NiO disappear and a new line is observed at $2\theta = 44.5^\circ$, corresponding to metallic Ni phase (PDF 4-850). Further heating up to 800 °C and isothermal period of 1h at this temperature led to an increase in the intensities of the characteristic lines of Ni^0 and CeO_2 . These results suggest a sintering of CeO_2 and Ni^0 crystallites during the reduction, as shown in Fig. 8B. The crystallite size of CeO_2 increased from 12 nm (580 °C) to 65 nm (800 °C for 1h), whereas the Ni^0 crystallite size grew from 5 nm (300 °C) to 33 nm (800 °C for 1h).

For Ni@CeO_2 and Ni@CeZrO_2 catalysts, only the typical lines of CeO_2 are observed below 500 °C. Above this temperature, the appearance of the lines corresponding to metallic Ni is noticed at 525 °C and 600 °C on the diffractograms of Ni@CeO_2 and Ni@CeZrO_2 catalysts, respectively. These results reveal that the reduction of nickel oxide is more difficult for the samples prepared by the sol-gel method, which is likely due to the strong interaction between

nickel oxide and CeO₂. These results agree with the TEM images and *in situ* XANES experiments, which showed that the embedded Ni particles in the ceria matrix are more hardly reduced than the segregated particles characteristic of the impregnated catalyst. The strong interaction between Ni and CeO₂ has been reported as an approach to improve the dispersion and avoid the metal sintering at high temperature [35]. Kathiraser et al. [36] studied the influence of Ce addition to Ni/SiO₂ catalysts for the oxidative reforming of biogas. They observed the increase in NiO reduction temperature with the presence of small amount of Ce (0.5 wt%) in the catalyst. This result was attributed to a higher interaction Ni-CeO₂ than Ni-SiO₂ as well as to a smaller NiO crystallite size as revealed by EXAFS. The TPR peaks of Ni@SiO₂ core-shell structure were shifted to higher temperatures in comparison to Ni/SiO₂ indicating that nickel oxide was hardly reduced in the core-shell structure [37]. This result was associated with a stronger metal-support interaction.

For Ni@CeO₂, the CeO₂ crystallite size increased during the reduction from 5 nm (325 °C) to 68 nm (800 °C for 1h), revealing a strong sintering at high temperature even for this sample prepared by the sol-gel method (Fig. 9B). A significant growth of the Ni⁰ crystallite size was also observed, increasing from 5 nm (630 °C) to 19 nm (800 °C for 1h).

In the case of Ni@CeZrO₂ catalyst, the CeO₂ crystallite size only slightly varied from 5 to 8 nm after reduction at 800 °C for 1h. The same trend was observed for the Ni⁰ crystallite size that increased from 5 to 10 nm at the end of the reduction (Fig. 10B).

The values of BET surface area of the samples before and after reduction (Table 1) showed that the addition of Zr into ceria structure significantly improved the thermal stability of the Ni@CeZrO₂ catalyst. The effect of type of dopant on the thermal stability and redox properties of ceria has been studied in the literature [20,38,39]. A higher thermal stability of CeZrO₂ in comparison to CeO₂ was attributed to the formation of a CeZr solid solution [28]. The samples aged at 1000 °C under reduction condition showed CeO₂ crystallite size equal to

73 and 39, for Pt/CeO₂ and Pt/Ce_{0.75}Zr_{0.25}O₂, respectively. In our work, the higher thermal stability of the ceria structure is likely due to the formation of the CeZrO₂ solid solution as revealed by XRD.

The increase in the reduction temperature led to a shift of the ceria lines to lower angles. The variation of CeO₂ lattice parameter during reduction of the samples is shown in Fig. 11. Increasing the reduction temperature increased the lattice parameter. The increase in the lattice parameter could be due to the thermal expansion as well as the change in the oxidation state of ceria from Ce⁴⁺ to Ce³⁺. In order to evaluate the effect of thermal expansion on the ceria lattice parameter during the reduction of all catalysts, an experiment was carried out with a physical mixture containing NiO and CeO₂ (Sigma-Aldrich) under air. The linear increase in the lattice parameter of NiO-CeO₂ up to 700 °C (see dotted line in Fig. 11) is attributed to the thermal expansion of the samples. However, the curves obtained for Ni/CeO₂, Ni@CeO₂ and Ni@CeZrO₂ catalysts deviates from this linear increase of the lattice parameter above 200 °C, indicating that the reduction of ceria began. Furthermore, a sharp increase in the lattice parameter was observed for Ni/CeO₂ and Ni@CeO₂ catalysts around 700 °C. The ceria reduction at low temperature region is generally attributed to the reduction of surface ceria, whereas the reduction at high temperature corresponds to the ceria bulk reduction [40]. The non-linear increase of the lattice parameter with the reduction temperature is likely due to the conversion of Ce⁴⁺ to Ce³⁺ [32]. Ce³⁺ ions have a higher ionic radius (1.034 Å) as compared to the Ce⁴⁺ ions (0.92 Å). Then, the formation of Ce³⁺ ions in ceria structure causes a change in the Ce-O bond length, which produces a lattice expansion and create oxygen vacancies [41]. The higher variation of lattice parameter for Ni@CeO₂ and Ni@CeZrO₂ suggests the formation of a higher number of oxygen vacancies on these catalysts during reduction.

The TPOIE experiments (Fig. 12) were performed to investigate the oxygen exchange capacity of the support as a function of temperature. The CeO₂ support only starts to exchange

oxygen at 380 °C, reaching the value of 39×10^{20} at.g⁻¹. The oxygen exchange begins at around 280 °C for Ni/CeO₂ catalyst and it occurs until $N_e = 35 \times 10^{20}$ at.g⁻¹ at 500 °C. For the embedded Ni@CeO₂ catalyst, the exchange started at lower temperature compared to the impregnated one (250 °C). At 500 °C, the number of exchanged oxygen atoms is 39×10^{20} at.g⁻¹. In comparison to Ni/CeO₂ and Ni@CeO₂ catalysts, the oxygen exchange begin at higher temperature for Ni@CeZrO₂ (300 °C) and the number of O atoms exchanged at 500 °C was 42×10^{20} at.g⁻¹. Da Silva et al. [39] have reported similar results for CeO₂ and CeNb supports. The catalysts showed similar isotopic distribution during the experiment (Fig. 13), indicating the occurrence of simple and multiple heteroexchange mechanisms [42].

The presence of metal decreases the energy required to start the exchange process compared with the CeO₂ support, because the exchange will occur mainly through the metal particle [43]. The doping of CeO₂ by ZrO₂ increases the temperature in which the exchange starts. This delay can be associated with a decrease in the surface oxygen concentration due to the lower specific surface area of CeZrO₂ compared to CeO₂. On the contrary there is a fast increase in the number of atoms exchanged for Ni@CeZrO₂, indicating that more oxygen atoms from the bulk phase are participating in the exchange process when Zr⁴⁺ is inserted into the CeO₂ structure. Therefore, the Ni@CeZrO₂ catalyst exhibited the highest number of oxygen exchanged compared with Ni/CeO₂ and Ni@CeO₂.

The experiments of isotopic oxygen exchange were carried out at 350, 400 and 450 °C. Figs. 14 and 15 illustrate the evolution of the number of exchanged atoms (N_e) and the isotopic distribution which occurs during the experiment at 400 °C. Table 3 reports the initial rate of exchange calculated from IOIE for the three temperatures. The exchange for CeO₂ is very low compared with the samples containing Ni, because the metal promotes the spillover of oxygen to ceria surface, as observed also in the TPOIE experiment. Comparing the Ni/CeO₂ and Ni@CeO₂ catalysts, the presence of Ni nanoparticles embedded on ceria structure does not

affect significantly the number of O atoms exchanged at the gas/solid equilibrium, but it increases significantly the initial rate of exchange, showing the positive influence of the close contact between Ni nanoparticles and ceria support (Table 3). The lower initial exchange rate and the higher N_e after 20 min reaction that are observed for Ni@CeZrO₂ catalyst confirms the results obtained in TPOIE experiment: a lower surface exchange activity compared to ceria-based samples but a higher bulk diffusion.

Indeed, the Ni@CeZrO₂ catalyst showed the highest number of N_e and the percentage of O atoms exchanged (Table 4). Furthermore, this catalyst exhibits a different behavior in the beginning of exchange at each temperature, with more formation of ³²O₂ than ³⁴O₂. On the opposite, Ni/CeO₂ and Ni@CeO₂ catalysts had a simultaneous formation of ³²O₂ and ³⁴O₂. Then, the Ni@CeZrO₂ catalyst favors the multiple exchange in comparison to the simple exchange at the beginning. Multiple heteroexchange occurs when two oxygen atoms are exchanged at the same time. Duprez et al. [42] observed the same behavior for Ce_{0.76}Zr_{0.32}O₂ samples, which was attributed to a higher concentration of superoxides species (O₂⁻) at the surface of the samples after oxidizing pre-treatment. Rossignol et al. [44] also correlated the presence of these species to the higher oxygen storage capacity when the Zr⁴⁺ is inserted in the ceria structure.

3.2. DRM reaction

The evolution of the CH₄ conversion, CO₂ conversion and H₂/CO molar ratio as a function of time on stream (TOS) at 800 °C are presented in Figs. 16A, 16B and 16C. The initial CH₄ and CO₂ conversions were approximately the same for all catalysts and they remained quite constant during 24 h of TOS. The reaction produces H₂ and CO with a H₂/CO molar ratio around 0.8. The CO₂ conversion was higher than the CH₄ conversion due to the occurrence of

reverse water gas shift reaction (Eq. 1.4), leading to the production of CO and H₂O and consequently, the H₂/CO ratio was lower than 1.0.

3.3. Characterization of used catalysts after DRM reaction

The main challenge on the design of a catalyst for the DRM reaction concerns the deactivation caused by carbon deposition. In order to investigate the formation of carbon during DRM reaction, the spent catalysts were characterized by SEM, TEM, Raman and TGA analysis.

SEM images of the catalysts after DRM at 800 °C for 24 h of TOS are displayed in Fig. 17. SEM image revealed the presence of carbon filaments on Ni/CeO₂ and Ni@CeO₂, mainly on the catalyst prepared by impregnation. On the other hand, carbon filaments were hardly detected on Ni@CeZrO₂ catalyst.

The TEM images of used catalysts shown in Fig. 18 can provide information about metal sintering as well as the formation of carbon filaments during the reaction. Ni/CeO₂ catalyst (Figs. 18 A and B) presented Ni nanoparticles without any interaction with CeO₂ matrix. Some Ni nanoparticles are located inside the carbon filaments, which avoid their sintering. There are also large nanoparticles outside the carbon nanotubes with particle size around 40 nm. For Ni@CeO₂ catalyst (Figs. 18 C and D), TEM images reveal the presence of Ni nanoparticles into CeO₂ bulk but sintering is observed (Ni particle size around 20 nm). This higher interaction inhibits the detachment of Ni particles from CeO₂ and the growth of carbon filament. The TEM images of Ni@CeZrO₂ (Figs. 18 E and F) show Ni nanoparticles embedded into ceria matrix with very small particle size (around 8 nm) after 24 h of TOS. Furthermore, carbon filaments are not observed, which demonstrate that inhibiting Ni sintering in the presence of a support with oxygen mobility suppress the formation of carbon filaments.

The Raman spectra of used catalysts exhibit two bands in the range of 1200 to 1800 cm⁻¹, which are indicative of carbon formation (Fig. 19). The G-band at 1581 cm⁻¹ is indicative of

ordered carbon, whereas the band at 1350 cm^{-1} (D-band) has been related to disordered carbon structures [45]. The D-band in the range of $1285\text{-}1300\text{ cm}^{-1}$ is ascribed to single-walled carbon nanotubes (SWCNT), while the position around 1330 cm^{-1} is related to multi-walled carbon nanotubes (MWCNT) or crystalline graphite-like forms [46,47]. The position of the D-band in 1350 cm^{-1} and the SEM images suggest the presence of MWCNT. Furthermore, the intensity of these bands was higher for Ni/CeO₂, indicating that the highest carbon deposition took place on this catalyst. These bands are barely detected on the spectrum of Ni@CeZrO₂, which suggests the presence of very low amount of carbon deposits on this catalyst, in agreement with the SEM image.

The derivative of weight during the TGA analysis is shown in Fig. 20. The DTG profile of Ni/CeO₂ sample exhibited an intense peak at $614\text{ }^{\circ}\text{C}$, whereas a broad peak at $518\text{ }^{\circ}\text{C}$ is observed in the DTG profile of Ni@CeO₂ catalyst. No peak was detected on the DTG profile of Ni@CeZrO₂, indicating that carbon was not deposited on this catalyst.

Table 5 reports the average rate of carbon formation for each catalyst during DRM reaction at $800\text{ }^{\circ}\text{C}$ for 24 h of TOS. Ni/CeO₂ catalyst exhibited the highest amount of carbon deposits but the carbon formation rate was significantly reduced for the catalysts containing Ni nanoparticles embedded in ceria structure. Ni@CeZrO₂ catalyst did not show evidences of carbon formation after DRM reaction.

3.4. The effect of Ni embedded in CeO₂ on catalyst deactivation for DRM

The mechanism of carbon formation over Ni-based catalysts during DRM has been extensively discussed in the literature [7,48,49] and involves the dissociation of methane on the surface of nickel particles, producing hydrogen and carbon (C_{α}). In the presence of a support with redox properties such as ceria and ceria-zirconia mixed oxides, this highly reactive carbon species (C_{α}) may reacts with oxygen from the support producing CO [46,50,51]. The unbalance

between the rate of methane decomposition and the reaction rate of carbon with oxygen from the support will lead to the accumulation of a less active carbon (C_{β}) that may also migrate into the nickel particle producing carbon filaments. Furthermore, the oxygen vacancies in the catalysts acts like active sites for CO_2 dissociative adsorption, which increase the amount of oxygen species on its surface. Therefore, the support plays an important role on the DRM reaction, keeping the metal surface free of carbon deposits. Yan et al. [52] recently demonstrated the importance of reactive oxygen species in close contact with Ni nanoparticles to oxidize the C_{α} before its polymerization for Ni/ CeO_2 - SiO_2 catalysts. The conversion of C_{α} species to CO by the reactive oxygen species could enhance the catalytic properties and stability of the Ni/ CeO_2 - SiO_2 catalyst. The same result was reported by Marinho et al. [50] for the steam reforming of ethanol over $LaNiO_3/CeSiO_2$ precursor catalyst. The strong metal-support interaction favored the transfer of oxygen from the support to metal through the metal-support interface. Roh et al. [53] successfully synthesized Ni catalyst supported on CeO_2 - ZrO_2 solid solution. They could observe the enhancement on catalyst stability for Ni/ $Ce_{0.8}Zr_{0.2}O_2$, which was due to the higher oxygen storage capacity and Ni dispersion. Yentekakis et al. [17] also proposed that $CeZrO_2$ support promotes the dissociative adsorption of CO_2 , producing a labile lattice oxygen that contributes to carbon oxidation.

Moreover, the rate of carbon formation is strongly affected by the Ni crystallite size [10]. The initiation step of carbon formation is more difficult over smaller particles. Then, carbon formation is minimized or inhibited on catalysts with small Ni particle sizes. Wang et al. [37] showed that the confinement of Ni nanoparticles inside SiO_2 spheres on Ni@ SiO_2 inhibited metal sintering during dry reforming of methane, minimizing carbon formation. Pu et al. [14] evaluated the influence of Ce on Ni@ Al_2O_3 core-shell catalysts to improve the coke resistance for steam reforming of acetic acid. The Ni@ Al_2O_3 core-shell structure could avoid metal sintering (Ni crystallite size < 5 nm) but carbon formation was observed yet. However,

the addition of Ce suppressed carbon deposition, which was attributed to the oxygen mobility of the material. The combination of small Ni size with oxygen mobility was fundamental to design a catalyst resistant to carbon formation.

In our work, the slight decrease in CH₄ and CO₂ conversions is likely due to the growth of Ni particle size as revealed by TEM. Furthermore, the inclusion of Ni nanoparticles into the CeZrO₂ structure for Ni@CeZrO₂ catalyst reduced metal sintering, as revealed by *in situ* XRD and TEM, due to the thermal stability of CeZrO₂ support during the reduction pre-treatment. In addition, this catalyst exhibited the highest number of O atoms exchanged during the isothermal oxygen isotopic exchange at 400 °C as well as the highest amount of oxygen vacancies formed as shown by XRD and Raman spectroscopy. Therefore, the control of Ni particle size and the high oxygen mobility of Ni@CeZrO₂ catalyst inhibited carbon deposition and favored the mechanism of carbon removal, promoting catalyst stability.

4. Conclusions

The one step preparation of Ni@CeO₂ and Ni@CeZrO₂ catalysts led to Ni nanoparticles embedded in the oxide, which had a positive effect on the stabilization of the Ni particle size during the reduction at high temperature (800 °C). It also generates more oxygen vacancies and increases the interaction with CeZrO₂ and CeO₂ in comparison with an impregnated catalyst Ni/CeO₂. Furthermore, doping of ceria with Zr could maintain the ceria structure throughout the thermal treatment and increase the mobility of oxygen in the material, compared to ceria alone, favoring the carbon removal mechanism during the reaction. Thus, the protection of the metal particle against sintering as well as the oxidation of carbon species by the support for the catalyst Ni@CeZrO₂ resulted in the suppression of carbon deposition during the DRM in our work.

5. Acknowledgements

The authors thank CNPq (Conselho Nacional de Desenvolvimento Científico e Tecnológico, Brazil, 308200/2014-7 and 303667/2018-4), CAPES (Coordenação de Aperfeiçoamento de Pessoal de Ensino Superior, Brazil, Finance code 001) and CAPES – COFECUB program (88881.142911/2017-01) for supporting this research and the scholarship received. The group also thanks the LNLS for the beamtime in DXAS and XPD experimental lines for the XANES and XRD analysis, respectively.

6. References

- [1] I.V. Yentekakis, G. Goula, Biogas Management: Advanced Utilization for Production of Renewable Energy and Added-value Chemicals, *Front. Environ. Sci.* 5 (2017) 7.
- [2] Y. Gao, J. Jiang, Y. Meng, F. Yan, A. Aihemaiti, A review of recent developments in hydrogen production via biogas dry reforming, *Energy Conversion and Management* 171 (2018) 133–155.
- [3] T.M. Gür, Comprehensive review of methane conversion in solid oxide fuel cells: Prospects for efficient electricity generation from natural gas, *Progress in Energy and Combustion Science* 54 (2016) 1–64.
- [4] H.N.C. da Silva, D.M. Prata, G.B.A. Lima, L.P. Zotes, L.V. Mattos, A techno-economic evaluation of the energy generation by proton exchange membrane fuel cell using biogas reforming, *Journal of Cleaner Production*, 200 (2018) 598-608.
- [5] L. Yang, X. Ge, C. Wan, F. Yu, Y. Li, Progress and perspectives in converting biogas to transportation fuels, *Renew. Sustain. Energy Rev.* 40 (2014) 1133–1152.
- [6] S.M. Stagg-Williams, F.B. Noronha, G. Fendley, D.E. Resasco, CO₂ reforming of CH₄ over Pt/ZrO₂ catalysts promoted with La and Ce oxides, *J. Catal.* 194 (2000) 240-249.

- [7] M.C.J. Bradford, M.A. Vannice, CO₂ reforming of CH₄, *Catal. Rev. - Sci. Eng.* 41 (1999) 1-42.
- [8] J. Rostrup-Nielsen, J.-H. Bak Hansen, CO₂ Reforming of Methane over Transition Metals, *J. Catal.* 144 (1993) 38–49.
- [9] P.M. Mortensen, I. Dybkjaer, Industrial scale experience on steam reforming of CO₂-rich gas, *Appl. Catal. A: General* 495 (2015) 141–151.
- [10] R.C. Rabelo-Neto, H.B.E. Sales, C.V.M. Inocência, E. Varga, A. Oszko, A. Erdohelyi, F.B. Noronha, L.V. Mattos, CO₂ reforming of methane over supported LaNiO₃ perovskite-type oxides, *Appl. Catal. B: Environ.* 221 (2018) 349–361.
- [11] M. Cargnello, N.L. Wieder, T. Montini, R.J. Gorte, P. Fornasiero, Synthesis of dispersible Pd@CeO₂ core-shell nanostructures by self-assembly, *J. Am. Chem. Soc.* 132 (2010) 1402–1409.
- [12] A.J. Majewski, J. Wood, Tri-reforming of methane over Ni@SiO₂ catalyst, *Int. J. Hydrog. Energy.* 39 (2014) 12578–12585.
- [13] C.S. Bonifacio, S. Carencio, C.H. Wu, S.D. House, H. Bluhm, J.C. Yang, Thermal Stability of Core–Shell Nanoparticles: A Combined in Situ Study by XPS and TEM, *Chem. Mater.* 27 (2015) 6960–6968.
- [14] J. Pu, Y. Luo, N. Wang, H. Bao, X. Wang, E.W. Qian, Ceria-promoted Ni@Al₂O₃ core-shell catalyst for steam reforming of acetic acid with enhanced activity and coke resistance, *Int. J. Hydrog. Energy.* 43 (2018) 3142–3153.
- [15] F. Wang, B. Han, L. Zhang, L. Xu, H. Yu, W. Shi, CO₂ reforming with methane over small-sized Ni@SiO₂ catalysts with unique features of sintering-free and low carbon, *Appl. Catal. B Environ.* 235 (2018) 26–35.
- [16] Q. Huang, X. Fang, Q. Cheng, Q. Li, X. Xu, L. Xu, W. Liu, Z. Gao, W. Zhou, X. Wang, Synthesis of a Highly Active and Stable Nickel-Embedded Alumina Catalyst for Methane

- Dry Reforming: On the Confinement Effects of Alumina Shells for Nickel Nanoparticles, *ChemCatChem*. 9 (2017) 3563–3571.
- [17] X. Wang, J.A. Rodriguez, J.C. Hanson, D. Gamarra, A. Martínez-Arias, M. Fernández-García, Ceria-based catalysts for the production of H₂ through the water-gas-shift reaction: Time-resolved XRD and XAFS studies, *Top. Catal.* 49 (2008) 81–88.
- [18] E.C. Faria, R.C.R. Neto, R.C. Colman, F.B. Noronha, Hydrogen production through CO₂ reforming of methane over Ni/CeZrO₂/Al₂O₃ catalysts, *Catal. Today* 228 (2014) 138–144.
- [19] S. Bedrane, C. Descorme, D. Duprez, Investigation of the oxygen storage process on ceria- and ceria – zirconia-supported catalysts, *Catal. Today* 75 (2002) 401–405.
- [20] P.P. Silva, F.A. Silva, L.S. Portela, L.V. Mattos, F.B. Noronha, C.E. Hori, Effect of Ce/Zr ratio on the performance of Pt/CeZrO₂/Al₂O₃ catalysts for methane partial oxidation, *Catal. Today* 107 (2005) 734–740.
- [21] I.V. Yentekakis, G. Goula, M. Hatzisymeon, I. Betsi-Argyropoulou, G. Botzolaki, K. Kousi, D.I. Kondarides, M.J. Taylor, C.M.A. Parlett, A. Osatiashtiani, G. Kyriakou, J.P. Holgado, R.M. Lambert, Effect of support oxygen storage capacity on the catalytic performance of Rh nanoparticles for CO₂ reforming of methane, *Appl. Catal. B Environ.* 243 (2019) 490–501.
- [22] A. Wolfbeisser, O. Sophiphun, J. Bernardi, J. Wittayakun, K. Föttinger, G. Rupprechter, Methane dry reforming over ceria-zirconia supported Ni catalysts, *Catal. Today* 277 (2016) 234–245.
- [23] E.T. Saw, U. Oemar, M.L. Ang, K. Hidajat, S. Kawi, Highly Active and Stable Bimetallic Nickel-Copper Core-Ceria Shell Catalyst for High-Temperature Water-Gas Shift Reaction, *ChemCatChem*. 7 (2015) 3358–3367.
- [24] Y. Wang, Y. Zhao, J. Lv, X. Ma, Facile synthesis of Cu@CeO₂ and its catalytic behavior for hydrogenation of methyl acetate to ethanol, *ChemCatChem*. 9 (2017) 2085–2090.

- [25] S.J.A. Figueroa, C. Prestipino, PrestoPronto: a code devoted to handling large data sets, *J. Phys. Conf. Ser.* 712 (2016) 12–16.
- [26] M. Li, A.C. van Veen, Tuning the catalytic performance of Ni-catalysed dry reforming of methane and carbon deposition via Ni-CeO_{2-x} interaction, *Appl. Catal. B Environ.* 237 (2018) 641–648.
- [27] H. Ay, D. Üner, Dry reforming of methane over CeO₂ supported Ni, Co and Ni-Co catalysts, *Appl. Catal. B Environ.* 179 (2015) 128–138.
- [28] C.E. Hori, H. Permana, K.Y.S. Ng, A. Brenner, K. More, K.M. Rahmoeller, D. Belton, Thermal stability of oxygen storage properties in a mixed CeO₂-ZrO₂ system, *Appl. Catal. B-Environ.* 16 (1998) 105–117.
- [29] T. Taniguchi, T. Watanabe, N. Sugiyama, A.K. Subramani, H. Wagata, N. Matsushita, M. Yoshimura, Identifying defects in ceria-based nanocrystals by UV resonance Raman spectroscopy, *J. Phys. Chem. C.* 113 (2009) 19789–19793.
- [30] A. Nakajima, ~ A Yoshihara, M. Ishigame, Defect-induced Raman spectra in doped CeO₂, *Phys. Rev. B.* 50 (1994) 13297–13307.
- [31] N. Mironova-Ulmane, A. Kuzmin, I. Steins, J. Grabis, I. Sildos, M. Pärns, Raman scattering in nanosized nickel oxide NiO, *J. Phys. Conf. Ser.* 93 (2007) 1–5.
- [32] L. Barrio, A. Kubacka, G. Zhou, M. Estrella, A. Martínez-Arias, J.C. Hanson, M. Fernández-García, J.A. Rodríguez, Unusual Physical and Chemical Properties of Ni in Ce_{1-x}Ni_xO_{2-y} Oxides: Structural Characterization and Catalytic Activity for the Water Gas Shift Reaction, *J. Phys. Chem. C.* 114 (2010) 12689–12697.
- [33] A. Bonk, A. Remhof, A.C. Maier, M. Trottmann, M.V.F. Schlupp, C. Battaglia, U.F. Vogt, Low-Temperature Reducibility of M_xCe_{1-x}O₂ (M = Zr, Hf) under Hydrogen Atmosphere, *J. Phys. Chem. C.* 120 (2015) 118–125.

- [34] A.I. Kozlov, H.K. Do, A. Yezerets, P. Andersen, H.H. Kung, M.C. Kung, Effect of preparation method and redox treatment on the reducibility and structure of supported ceria-zirconia mixed oxide, *J. Catal.* 209 (2002) 417–426.
- [35] W. Zheng, J. Zhang, Q. Ge, H. Xu, W. Li, Effects of CeO₂ addition on Ni/Al₂O₃ catalysts for the reaction of ammonia decomposition to hydrogen, *Appl. Catal. B Environ.* 80 (2008) 98–105.
- [36] Y. Kathiraser, Z. Wang, M.L. Ang, L. Mo, Z. Li, U. Oemar, S. Kawi, Highly active and coke resistant Ni/SiO₂ catalysts for oxidative reforming of model biogas: Effect of low ceria loading, *J. CO₂ Util.* 19 (2017) 284–295.
- [37] F. Wang, L. Xu, W. Shi, Syngas production from CO₂ reforming with methane over core-shell Ni@SiO₂ catalysts, *J. CO₂ Util.* 16 (2016) 318–327.
- [38] J. Kašpar, P. Fornasiero, M. Graziani, Use of CeO₂-based oxides in the three-way catalysis, *Catal. Today.* 50 (1999) 285–298.
- [39] A.A.A. da Silva, N. Bion, F. Epron, S. Baraka, F.C. Fonseca, R.C. Rabelo-Neto, L.V. Mattos, F.B. Noronha, Effect of the type of ceria dopant on the performance of Ni/CeO₂ SOFC anode for ethanol internal reforming, *Appl. Catal. B Environ.* 206 (2017) 626–641.
- [40] V. Perrichon, A. Laachir, G. Bergeret, R. Fréty, L. Tournayan, O. Touret, Reduction of ceria with different textures by hydrogen and their reoxidation by oxygen, *J. Chem. Soc. Faraday Trans.* 90 (1994) 773–781.
- [41] M. Piumetti, S. Bensaid, D. Fino, N. Russo, Nanostructured ceria-zirconia catalysts for CO oxidation: Study on surface properties and reactivity, *Appl. Catal. B Environ.* 197 (2016) 35–46.
- [42] Y. Madier, C. Descorme, A.M. Le Govic, D. Duprez, Oxygen Mobility in CeO₂ and Ce_xZr_(1-x)O₂ Compounds: Study by CO Transient Oxidation and ¹⁸O/¹⁶O Isotopic Exchange, *J. Phys. Chem. B.* 103 (1999) 10999–11006.

- [43] D. Martin, D. Duprez, Mobility of Surface Species on Oxides. 1. Isotopic Exchange of $^{18}\text{O}_2$ with ^{16}O of SiO_2 , Al_2O_3 , ZrO_2 , MgO , CeO_2 , and $\text{CeO}_2\text{-Al}_2\text{O}_3$. Activation by Noble Metals. Correlation with Oxide Basicity, *J. Phys. Chem.* 100 (1996) 9429–9438.
- [44] S. Rossignol, F. Gérard, D. Duprez, Effect of the preparation method on the properties of zirconia-ceria materials, *J. Mater. Chem.* 9 (1999) 1615–1620.
- [45] W.E. Alvarez, F. Pompeo, J.E. Herrera, L. Balzano, D.E. Resasco, Characterization of single-walled carbon nanotubes (SWNTs) produced by CO disproportionation on Co-Mo catalysts, *Chem. Mater.* 14 (2002) 1853-1858.
- [46] O.C.V. Silva, E.B. Silveira, R.C. Rabelo- Neto, L.E.P. Borges, F.B. Noronha, Hydrogen Production Through Steam Reforming of Toluene Over Ni Supported on MgAl Mixed Oxides Derived from Hydrotalcite-Like Compounds, *Catal. Letters.* 148 (2018) 1622–1633.
- [47] T. Belin, F. Epron, Characterization methods of carbon nanotubes: a review, *Mater. Sci. Eng. B.* 119 (2005) 105–118.
- [48] P. Ferreira-Aparicio, Mechanistic aspects of the dry reforming of methane over ruthenium catalysts, *Appl. Catal. A* 202 (2000) 183–196.
- [49] J. Wei, E. Iglesia, Isotopic and kinetic assessment of the mechanism of reactions of CH_4 with CO_2 or H_2O to form synthesis gas and carbon on nickel catalysts, *J. Catal.* 224 (2004) 370–383.
- [50] A.L.A. Marinho, R.C. Rabelo-Neto, F.B. Noronha, L. V. Mattos, Steam reforming of ethanol over Ni-based catalysts obtained from LaNiO_3 and $\text{LaNiO}_3/\text{CeSiO}_2$ perovskite-type oxides for the production of hydrogen, *Appl. Catal. A* 520 (2016) 53–64.
- [51] F.B. Noronha, E.C. Fendley, R.R. Soares, W.E. Alvarez, D.E. Resasco, Correlation between catalytic activity and support reducibility in the CO_2 reforming of methane over $\text{Pt/Ce}_x\text{Zr}_{1-x}\text{O}_2$ catalysts, *Chem. Eng. J.* 82 (2001) 21–31.

- [52] X. Yan, T. Hu, P. Liu, S. Li, B. Zhao, Q. Zhang, W. Jiao, S. Chen, P. Wang, J. Lu, L. Fan, X. Deng, Y. X. Pan, Highly efficient and stable Ni/CeO₂-SiO₂ catalyst for dry reforming of methane: Effect of interfacial structure of Ni/CeO₂ on SiO₂, *Appl. Catal. B Environ.* 246 (2019) 221–231.
- [53] H.-S. Roh, K.Y. Koo, U.D. Joshi, W.L. Yoon, Combined H₂O and CO₂ Reforming of Methane Over Ni–Ce–ZrO₂ Catalysts for Gas to Liquids (GTL), *Catal. Lett.* 125 (2008) 283–288.

Accepted manuscript

Figure Caption

Figure 1. TEM images and EDX of selected areas of Ni/CeO₂, Ni@CeO₂ and Ni@CeZrO₂ catalysts after reduction at 800 °C.

Figure 2. Raman spectra for the calcined samples and a CeO₂ reference.

Figure 3. XANES spectra obtained during the reduction of Ni/CeO₂ catalyst.

Figure 4. XANES spectra obtained during the reduction of Ni@CeO₂ catalyst.

Figure 5. XANES spectra obtained during the reduction of Ni@CeZrO₂ catalyst.

Figure 6. Fraction of Ni⁰ calculated by the linear combination of Ni K-edge XANES spectra of references during the reduction for all catalysts.

Figure 7. X-ray diffraction patterns of calcined samples: (A) Ni/CeO₂; (B) Ni@CeO₂; and (C) Ni@CeZrO₂.

Figure 8. (A) X-ray diffraction patterns obtained during reduction from room temperature to 800 °C for Ni/CeO₂; (B) Crystallite size of NiO, Ni⁰ and CeO₂ during the reduction process.

Figure 9. (A) X-ray diffraction patterns obtained during reduction from room temperature to 800 °C for Ni@CeO₂; (B) Crystallite size of Ni⁰ and CeO₂ during the reduction process.

Figure 10. (A) X-ray diffraction patterns obtained during reduction from room temperature to 800 °C for Ni@CeZrO₂; (B) Crystallite size of Ni⁰ and CeO₂ during the reduction process.

Figure 11. Variation of CeO₂ lattice parameter as a function of reduction temperature for all catalysts; (---) NiO-CeO₂ physical mixture; (●) Ni/CeO₂; (▲) Ni@CeO₂; (▼) Ni@CeZrO₂.

Figure 12. Evolution of the number of exchanged oxygen atoms during TPOIE over Ni/CeO₂, Ni@CeO₂, Ni@CeZrO₂ and CeO₂.

Figure 13. Isotopic distribution during the TPOIE for Ni/CeO₂, Ni@CeO₂, Ni@CeZrO₂ and CeO₂.

Figure 14. Evolution of the number of exchanged oxygen atoms during IOIE at 400 °C over CeO₂, Ni/CeO₂, Ni@CeO₂ and Ni@CeZrO₂.

Figure 15. Isotopic distribution during the IOIE at 400 °C.

Figure 16. (A) CH₄ conversion, (B) CO₂ conversion and (C) H₂/CO molar ratio versus TOS for dry reforming at 800 °C.

Figure 17. SEM images of spent catalysts after DRM at 800 °C for 24 h of TOS.

Figure 18. TEM images of spent catalysts after DRM at 800 °C for 24 h of TOS; (A) and (B) Ni/CeO₂; (C) and (D) Ni@CeO₂; (E) and (F) Ni@CeZrO₂.

Figure 19. Raman spectra of post-reaction catalysts.

Figure 20. DTG of the post-reaction samples.

Accepted manuscript